Supplementary Information

Manipulating unidirectional fluid transportation to drive sustainable solar water extraction and brine-drenching induced energy generation

Yaoxin Zhang,[a, †] Hong Zhang,[a, †] Ting Xiong,[a] Hao Qu,[a] J. Justin Koh,[a] Dilip Krishna Nandakumar,[a] John Wang,[a] Swee Ching Tan[a, *]

Affiliations

[a] Department of Materials Science and Engineering, National University of Singapore, 9 Engineering drive 1, Singapore 117574.

† These authors contributed equally to this work.

* Corresponding author. Email: msetansc@nus.edu.sg

Table of Content:

Supplementary Figures

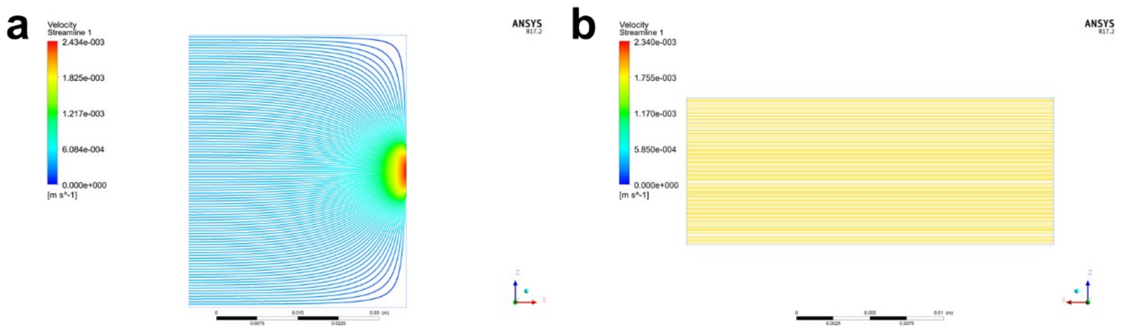

Fig. S1 Simulative results showing the water transport pathways of fluidic model with narrow (a) and equally wide outlet channels under high feed rate (20-fold). Streamline patterns are same as the results revealed in **Fig. 1**, suggesting that narrow outlet would lead to salt formation at the two corners next to the discharge portal.

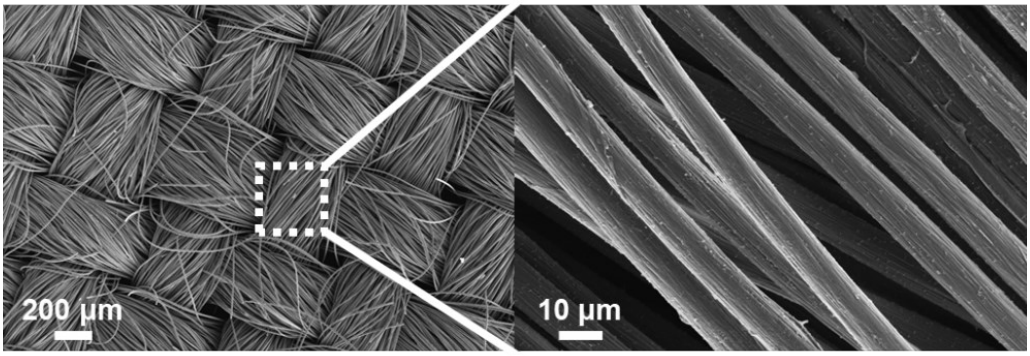

Fig. S2 SEM images of pristine carbon cloth showing smooth fibrous texture.

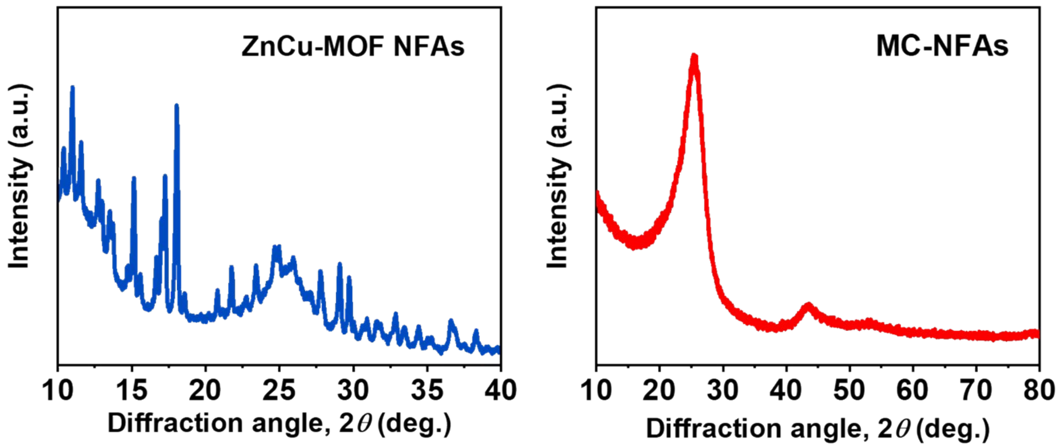

Fig. S3 XRD patterns of ZnCu-MOF precursor (left) and MOF-derived MC-NFAs structure (right) indicating the successful derivation of mesoporous carbon from ZnCu-MOF precursors.

©

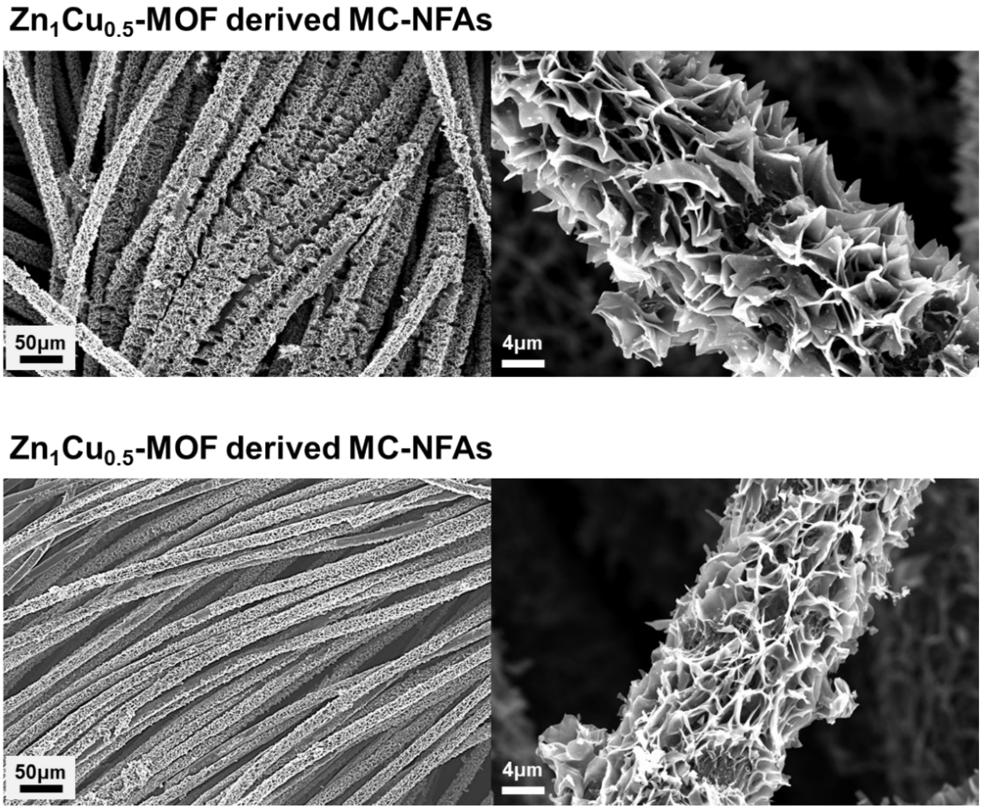

Fig. S4 SEM images showing structures of MC prepared with different ratio of Zn/Cu in MOF precursors (1:0.5 and 1:1).

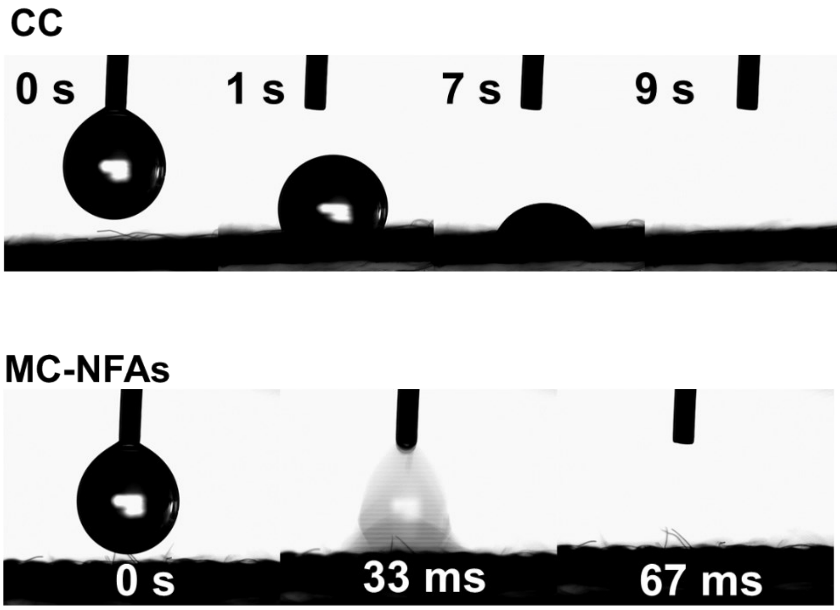

Fig. S5 Contact angle measurements demonstrating the improved wettability of the as-prepared MC-NFAs in comparison to CC, which would not only ensure sufficient water supply for solar extraction process, but also facilitate water transportation to avoid salt crystallization that is caused by sluggish brine flow.

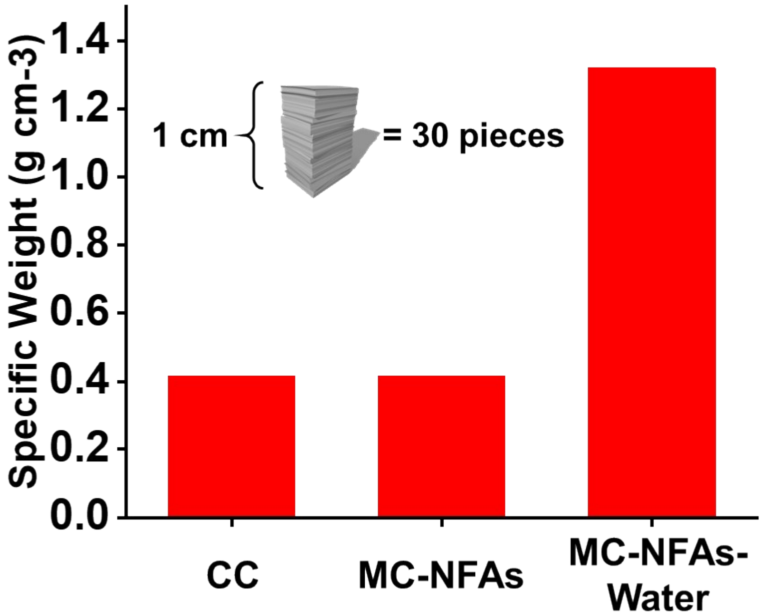

Fig. S6 Specific weight change of MC-NFAs compared to pristine CC. The growth of MC-NFAs on CC led to negligible weight change, but the improved surface hydrophilicity allows it to highly absorb water. It is also worth noting that MC-NFAs is only 0.33mm thick, which means a stack of MC-NFAs sheets would take up minimal space. This merit would allow it to be portable and easy for transportation.

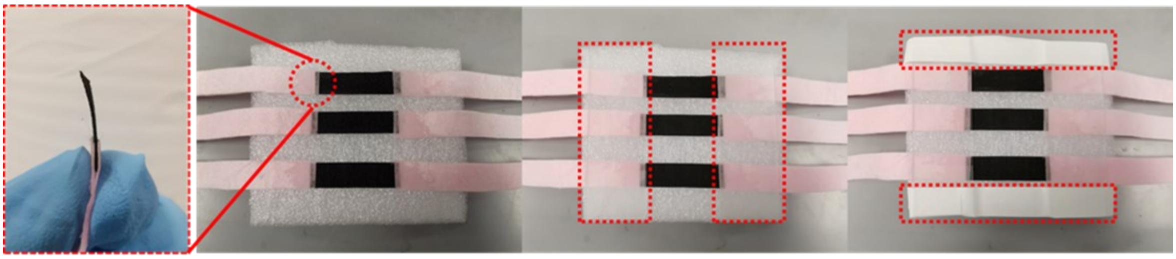

Fig. S7 Assembly of fluidic photothermal structure. Each end of a long and narrow piece of MC-NFAs was firstly clipped by capillary wicking belts (in pink colour) to allow MC-NFAs to receive fluid symmetrically. The connection parts were then immobilized successively by two glass slabs (indicated by vertical red rectangles) and tapes (indicated by horizonal red rectangles).

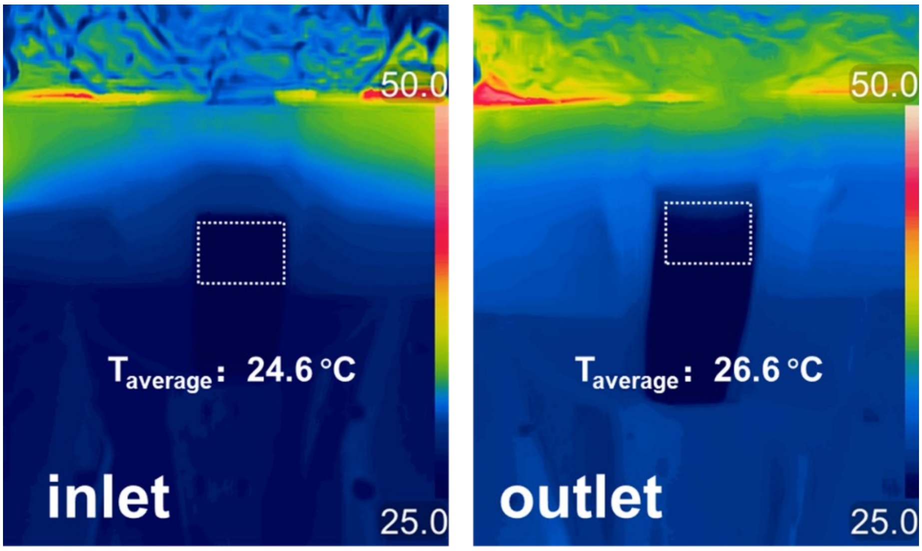

Fig. S8 IR images indicating the temperature of the inlet belt and the outlet belt for estimation of heat loss to brine fluid, which is based on the following equation:

$$R_e = \frac{uAtC(T_{outlet} - T_{inlet})}{P_0}$$

where u is the flow speed of outlet, A refers to the section area of outlet, t is the operation time, C is the specific heat of discharge brine, T_{outlet} and T_{inlet} are respectively the average temperature of discharge (outlet) and feed solution (inlet), P_0 is the total solar energy input throughout the operation,

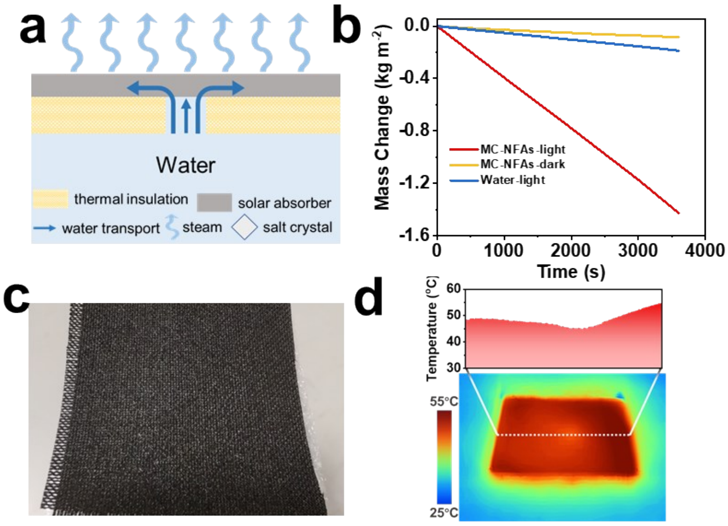

Fig. S9 Solar evaporation in conventional configuration with 1D water transport pathway by using pure water. The 1D water transport was enabled by a capillary wick. **a** Configuration of pure wate evaporation. **b** Mass change of MC-NFAs and pure water under light (1 sun) and dark conditions. **c** Physical picture of MC-NFAs sheet after continuous operation. **d** Surface temperature mapping of MC-NFAs under 1 sun illumination.

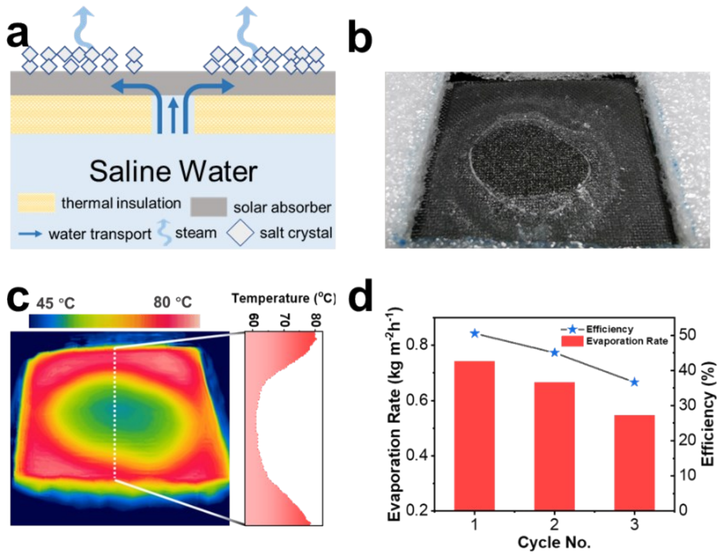

Fig. S10 Solar evaporation in conventional configuration with 1D water transport pathway by using saline water (3.5 wt%). The 1D water transport was enabled by a capillary wick. **a** Configuration of saline wate evaporation. Unlike pure water evaporation, salt accumulates on the surface of evaporator, thus suppressing further water vapor generation. **b** Physical picture of MC-NFAs sheet after continuous desalination showing the accumulated salt on its surface. **c** Surface temperature mapping of MC-NFAs under 1 sun illumination. Due to the salt crust, surface temperature of MC-NFAs becomes uneven. d Evaporation rate and corresponding efficiency of MC-NFAs measured after the formation of surface salt showing the sharply diminished performance.

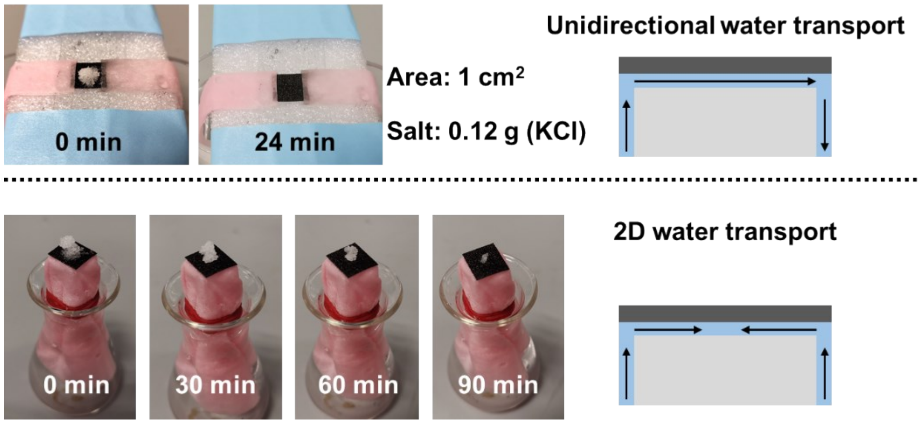

Fig. S11 Progressions of salt rejection by unidirectional water transport and conventional 2D water transport. The results show that unidirectional water flow is more effective in salt removal, suggesting salt clogging is less likely to happen to this fluidic structure during heavy brine desalination.

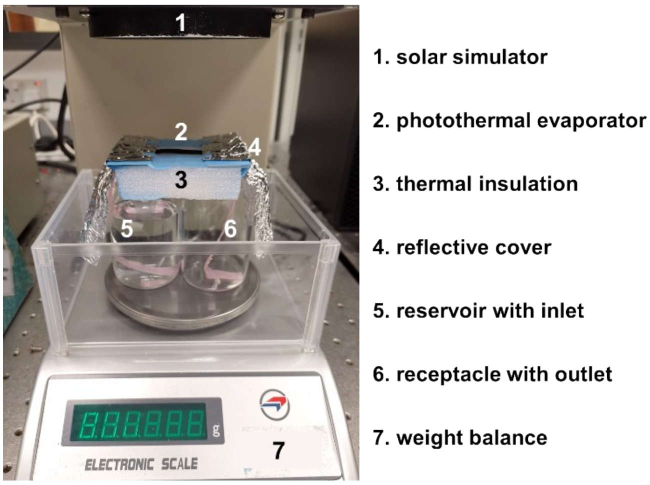

Fig. S12 Experimental setup for precise measurements of solar water extraction.

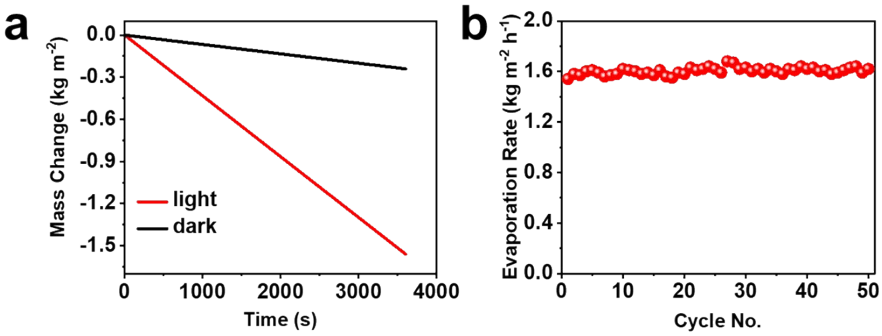

Fig. S13 Solar water extraction performance in fluidic photothermal configuration. **a** Mass change of MC-NFAs under light (1 sun) and dark conditions. **b** 50 continuous operation cycles showing the excellent stability of the proposed structure for high-efficiency and salt-rejecting photothermal conversion.

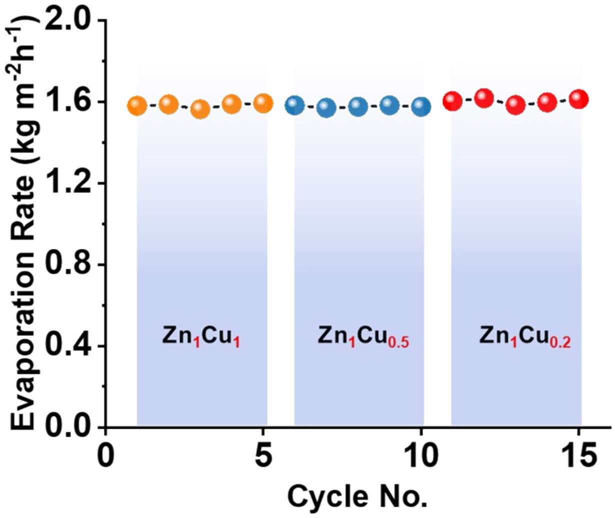

Fig. S14 Performance comparisons between MC-NFAs derived respectively from Zn_1Cu_1-MOF, $Zn_1Cu_{0.5}$-MOF and $Zn_1Cu_{0.2}$-MOF precursors.

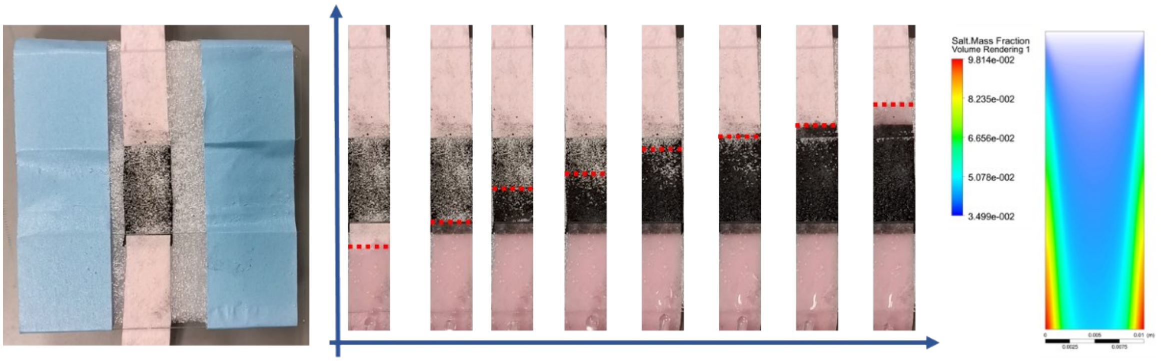

Fig. S15 Experimental and simulative verification of boundary conditions of side walls of MC-NFAs. The type of the boundary condition of side walls, including free slip wall and non-free slip wall, determines the later conclusions drawn from simulation analysis. To decide which type suits our model, a diffusion test was carried out. The fluid interface highlighted by red dot line raised in a stepwise pattern, and no sharp gradient caused by the boundary wall was observed, suggesting the wall type is free slip. Reduction to absurdity was also adopted to prove it. In the simulation with non-free slip wall conditions, the salt mass fraction of the edge tends to be higher than the middle area, and thus salt would accumulate chronically. However, experimental observations showed that for continuous desalination, no salt was spotted at the edges, which indicates that non-free slip wall is not the correct

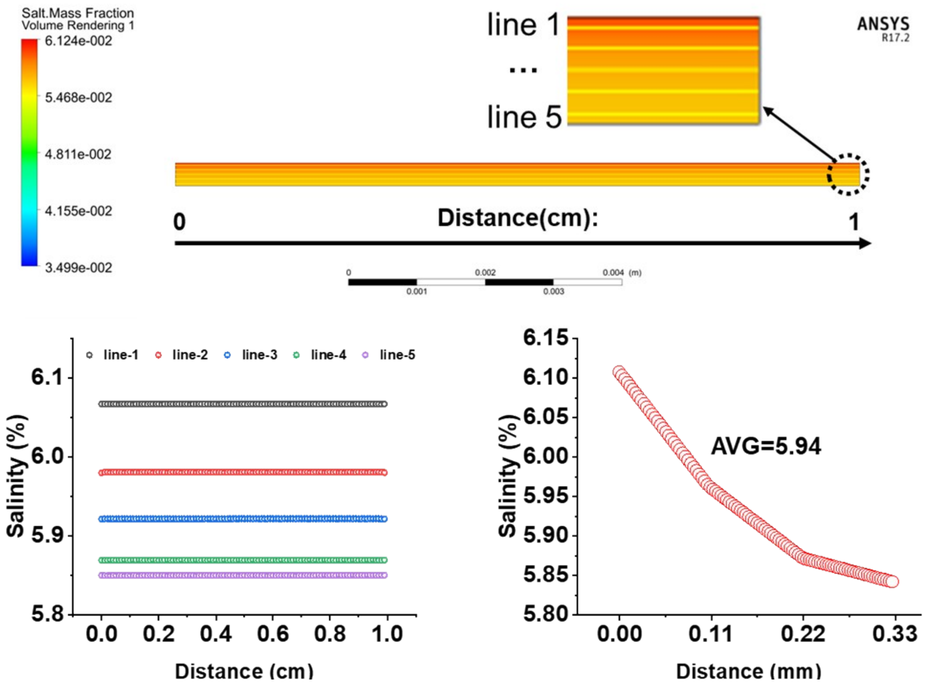

Fig. S16 Determination of discharge salinity by analytical results from CFD simulation. Since water is extracted from the top surface of MC-NFAs while no water loss from the backside, a salt concentration gradient is formed at the cross section from where the treated brine discharges into the outlet. To decide the discharge salinity, five horizontal lines were firstly defined on the cross section, and results show that the salinity along each line is constant, allows for direct calculation of the overall salinity with the longitudinal gradient, which is 5.94 wt% on the average.

a
b
c

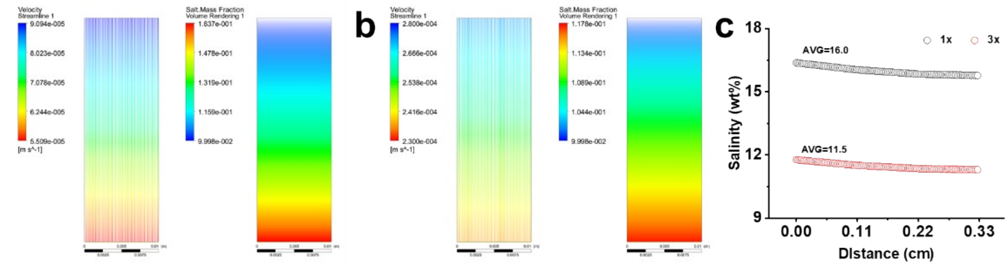

Fig. S17 Feed rate (10 wt%) effect on discharge salinity. Water pathway profile (left) and salt mass fraction pattern (right) of CFD model with constant flux of 9.53 ml $cm^{-2}s^{-1}$ (**a**) and 3 x 9.53 ml $cm^{-2}s^{-1}$(**b**). The flux of 9.53 m cm^{-2} s^{-1} was determined according to experimental observations. **c** Discharge salinity profiles along the gradient of the cross sections of outlets in the two cases. It shows that tripling the initial feed rate decreases the discharge salinity from 16 wt% down to 11.5 wt%.

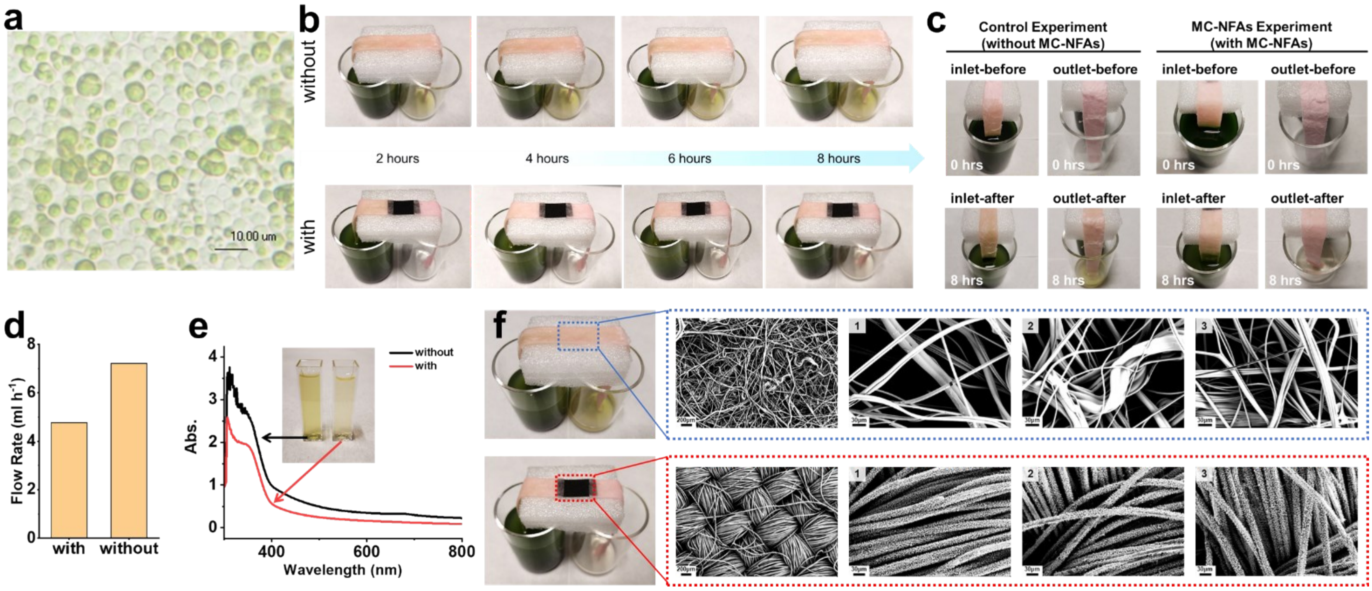

Fig. S18 Anti-biofouling tests of the proposed fluidic structure with control experiments by using concentrated algae suspension. **a** Microscopic image of algae solution. The size of algae cells ranges from 1~10 μm. **b** Physical pictures of the fluidic setup with and without MC-NFAs fabric in the process of filtration experiments (8 hours). **c** Inlet and outlet comparisons before and after 8 hours' filtration. **d** Flow rates of anti-biofouling experiments with and without MC-NFAs. **e** UV-Vis spectra of the discharge water obtained after filtration e f UV-Vis spectra of the initial algae solution and the discharge solution. **f** SEM images of the capillary wicking strip and MC-NFAs fabric after 8 hours' anti-biofouling experiments. 3 random sites were selected on each sample for SEM imaging, in order to ensure whether or not the sample was attached by algae cells.

It can be seen that in both experiments, the green algae were almost completely blocked by the inlet feed strips while no algae attached on the outlet was observed, indicating that the anti-biofouling process was mostly due to the capillary strips instead of MC-NFAs fabric. At the same time, we also noticed that after 8 hours operation, the volumes of the discharge water were different. With MC-NFAs, the flow rate was found lower than that without the fabric. It is probably because the thin MC-NFAs fabric with relatively low permeability slows down the running fluid. The discharge water obtained without MC-NFAs was darker than that with MC-NFAs, as shown in the UV-Vis spectra, which is probably because the slow flow rate and nanostructures of the MC-NFAs enhanced the filtration performance. But it should be noted that there were no algae present in these two discharge water samples as we did not observe any algae cells on the same segment from both experiments as SEM images show. The dark colour of the discharge water from the control experiment might be due to nanoscale impurities from algae (e.g. algae organelles). Furthermore, the overall absorption (with MC-NFAs) was even higher than the result shown in Figure 4g (main text). We believe this was caused by the accumulated soluble dye and colorants in the concentrated algae suspension.

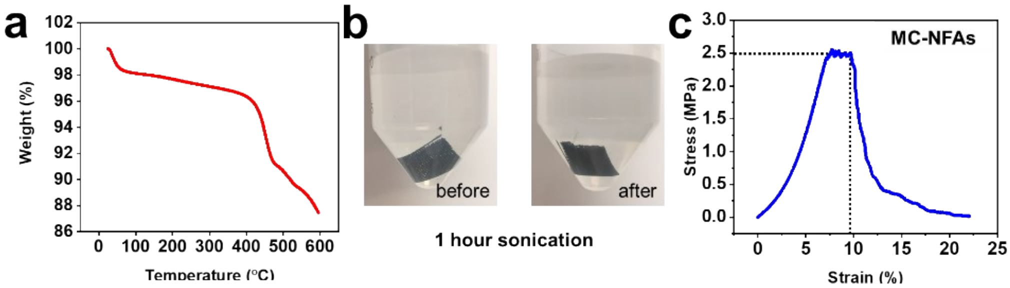

Fig. S19 Thermal and mechanical stability of MC-NFAs. **a** TGA analysis. **b** Physical pictures of MC-NFAs before and after 1-hour sonication showing no significant exfoliation. **c** Tensile stress-strain diagram of MC-NFAs.

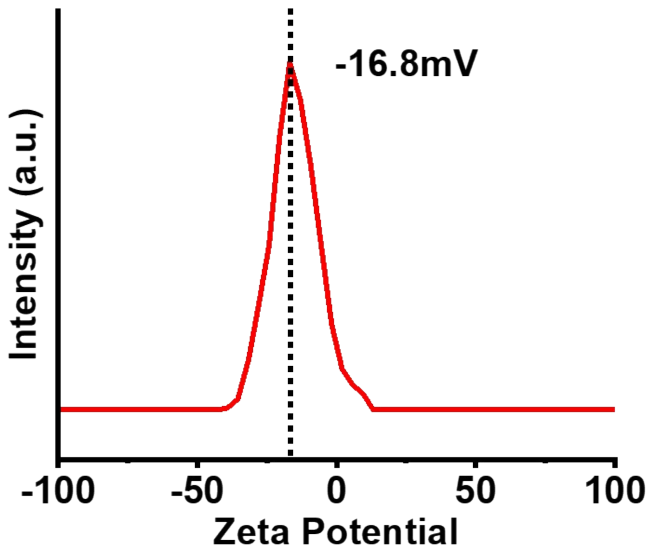

Fig. S20 Zeta potential of the as-prepared carbon ink, indicating the surface of the carbon materials is negatively charged, which allows to adsorb cations and form EDL layer at the materials/water interface.

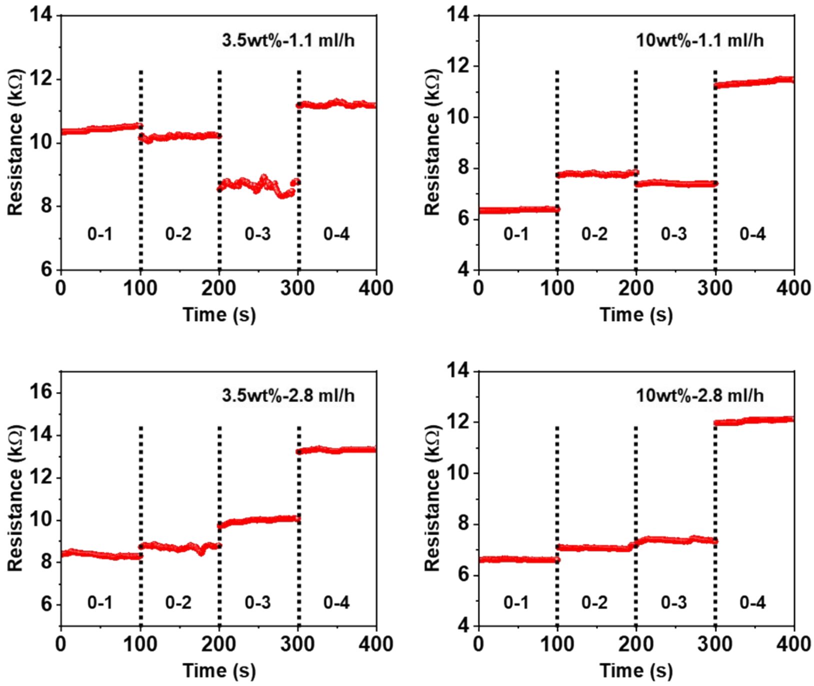

Fig. S21 Resistance of WEG in response to brine fluid with different salinity and flux rate. All the tests were conducted by measuring the resistance between point 0 and 1.

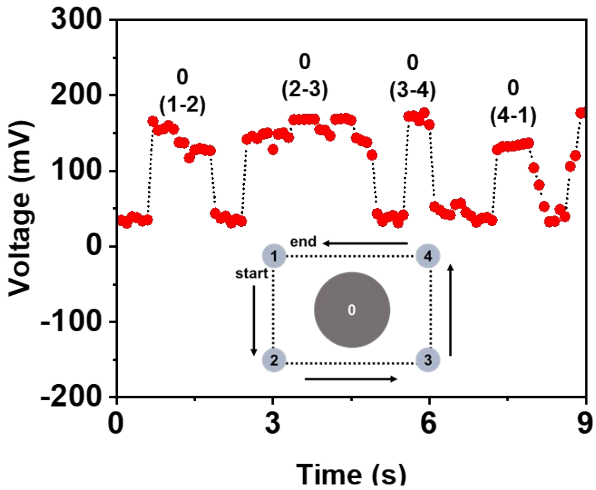

Fig. S22 Voltage measured between point 0 and the other moving testing point following the route indicated from the inset illustration. The movement speed might vary during measurement.

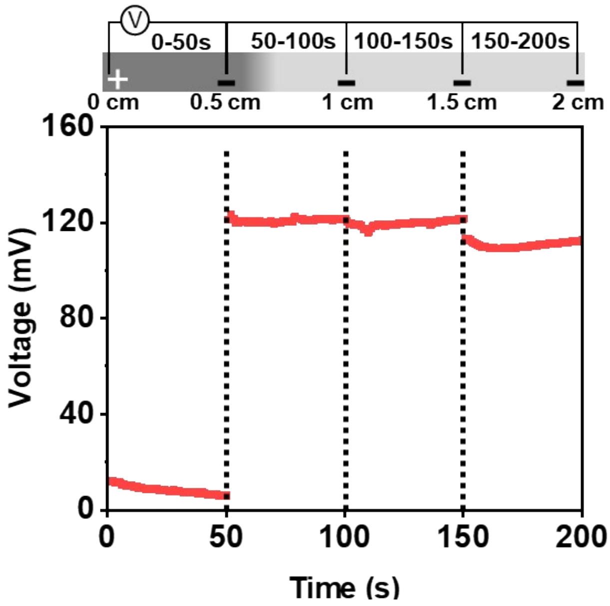

Fig. S23 Voltage of WEGs in response to linear mass loading gradient showing distinct difference and distance dependence. This property facilitates stable electric connections and power output.

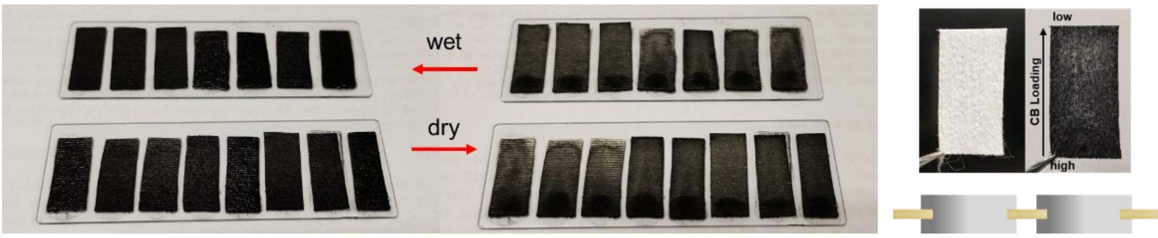

Fig. S24 Mass fabrication of WEGs for power supply. It can be seen in dry condition, WEGs show clear linear gradient of mass loading, which allows for simple connection for scaled up electrical output.

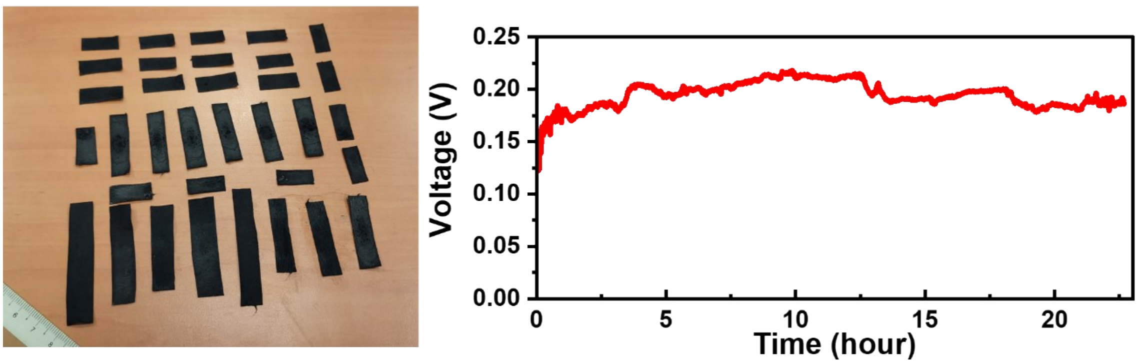

Fig. S25 Stability test of WEG. To investigate the stability, more WEGs were fabricated in this revision as shown in the Figure S23 (left). Most of their voltage are in the range of 100 mV and 200 mV, but stabilizing at ~200 mV is possible to achieve as the right graph shows, in which stability test lasting over 20 hours was demonstrated. It was observed from a WEG sample that was highly loaded with CB-SDBS at one end of it. Future improvements on the performance of WEG are likely to get realized via loading gradient adjustment, materials modification and structure engineering.

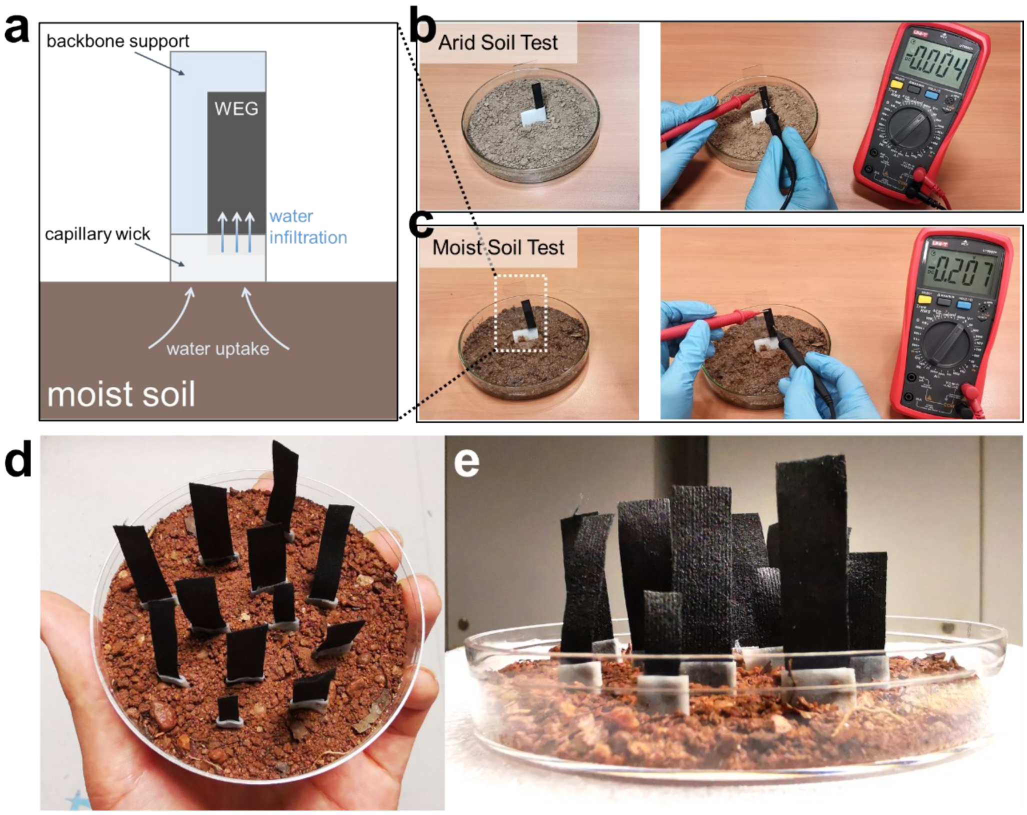

Fig. S26 Artificial grass (WEGs) for ground water detection and energy generation. **a** Working principle of artificial grass (WEGs). **b** arid soil test showing no electric induction. **c** moist soil test showing electricity induction. **d-e** Physical pictures showing the artificial greensward by planting WEGs into soil. By inserting WEGs into ground, which is shown in the Figure S26, electricity is induced with water harvested from the moist soil, and when the water content of soil is low as the arid soil test shows, the electrical signal is negligible. With this property, WEG can be employed to detect the soil water content, and it would be particularly useful to farmers. Suppose the farmland is lack of water, WEG is subjected to electrical outage, which would be a strong reminder to farmers that agricultural irrigation should be scheduled. It is also possible to extensively plant WEGs on ground like grasses. This artificial greensward is able to harvest water from soil for large-scale electricity generation.

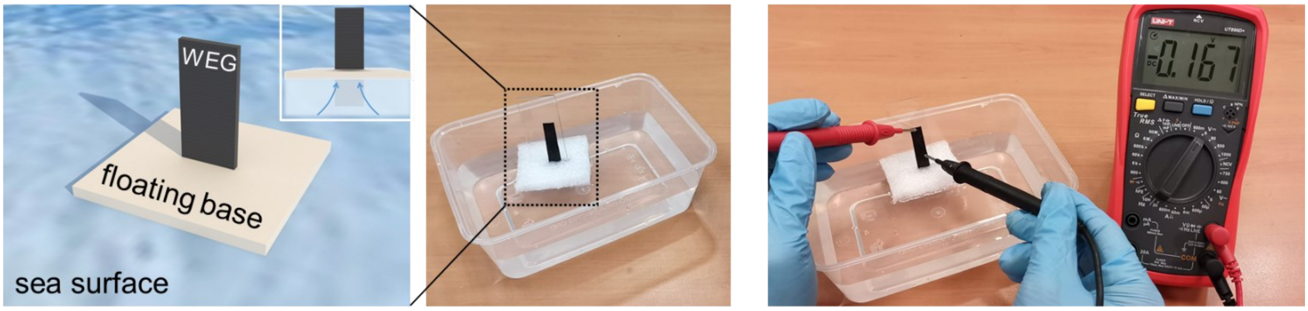

Fig. S27 Direct and constant electricity generation of floating WEG on sea surface. Similar to the working mode of WEG via ground water harvesting, the proposed floating WEG generates electricity directly with seawater. The lightweight base makes the floating WEG a standalone system, and the capillary tail-like part of the WEG fabric, which is immersed below water level, keeps the whole fabric wet, therefore, WEG would operate constantly. Additionally, the WEG is vertically attached to a backbone support (e.g. glass slide), thus even an amount of WEGs would takes up minimal area of sea surface.

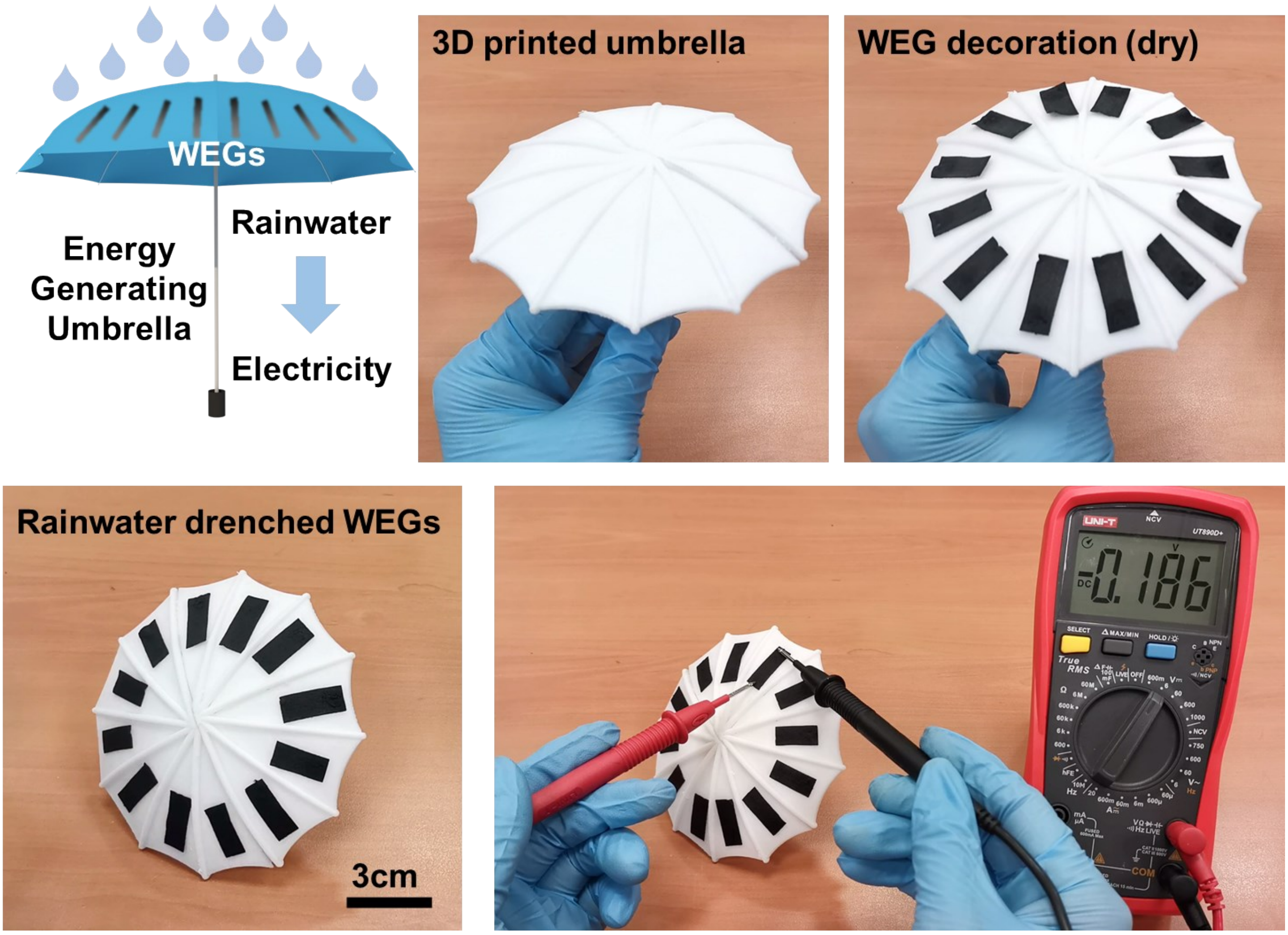

Fig. S28 Energy harvesting from rainwater by decorating umbrella with WEGs. Rain is a natural water source and can be ideally used to trigger the drenching of WEG for mobile energy generation. To demonstrate it, we have 3D printed a minitype umbrella by using acrylonitrile butadiene styrene (ABS) as shown in Figure S28. WEG fabrics were readily decorated on the umbrella surface in an aesthetical pattern. The attached WEGs, after drenched by rainwater, is capable of continuous electricity output. This interesting WEG-integrated umbrella enables energy harvesting on the rainy days and serves as portable power source, and we believe it is possible to further combine with TENGs for enhanced and long-lasting energy generation.

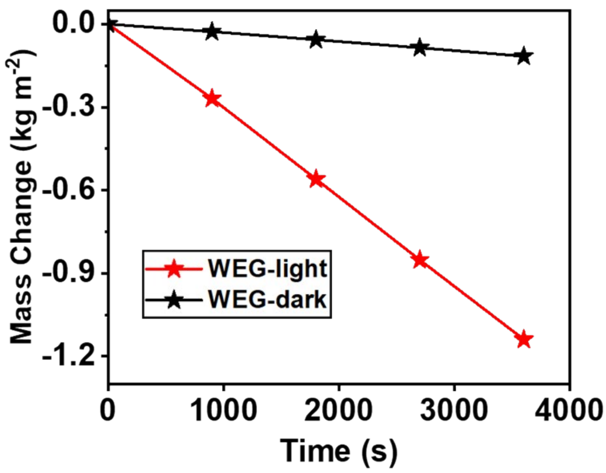

Fig. S29 Mass change of WEG device as solar water extractor. It is shown that compared to MC-NFAs (>1.6 kg m^{-2} h^{-1}), WEG delivers a much lower evaporation rate (~1.1 kg m^{-2} h^{-1}).

Supplementary Table

Table S1. Advantages and disadvantages of different salt-rejection strategies.

Salt-rejection Strategies	Advantages	Disadvantages
Physical Wash and Rinse	• Fast	• External interventions causing extra operation cost • Discontinuous evaporation • Not suitable to bulk and thick evaporators • Efficiency decreases when salt starts accumulating.
Self-dissolution	• Self-sustained	• Time consuming • Discontinuous evaporation • Reduced operation time if salt forms during daytime, leading to limited water yields • Efficiency decreases when salt starts accumulating
Fluid Convection	• Self-sustained • Continuous evaporation • Efficiency can be maintained	• Low efficiency due to large water contact
Hydrophobic Design	• Self-sustained • Continuous evaporation • Efficiency can be maintained	• Low efficiency as evaporation takes place at water surface
Unidirectional fluid	• Minimal contact with water leads to high efficiency • Efficiency can be maintained • Continuous evaporation	• External interventions may be needed to keep hydraulic driving force

Supplementary Movie Captions

Movie S1

Demonstration of unidirectional fluid flow in the fluidic photothermal structure. The fluid was colored by blue food dye to indicate the transportation pathways.

Movie S2

Voltage measurements between the as-defined test points of a WEG device before and after being drenched by 3.5 wt% brine water.

Movie S3

Demonstration of powering a digital watch with 11 WEGs connected in series. All the WEGs were drenched by 3.5 wt% brine water.

Movie S4

Sweat-drenching induced electricity generation with WEG on human skin.

Movie S5

The integrated system of fluidic photothermal structure and WEG for simultaneous clean water extraction and electricity generation.